We are IntechOpen, the world's leading publisher of Open Access books Built by scientists, for scientists

4,800
Open access books available

122,000
International authors and editors

135M
Downloads

Our authors are among the

154
Countries delivered to

TOP 1%
most cited scientists

12.2%
Contributors from top 500 universities

CLARIVATE ANALYTICS
BOOK
CITATION
INDEX
INDEXED

WEB OF SCIENCE™

Selection of our books indexed in the Book Citation Index
in Web of Science™ Core Collection (BKCI)

Interested in publishing with us?
Contact book.department@intechopen.com

Numbers displayed above are based on latest data collected.
For more information visit www.intechopen.com

Grain-Scale Modeling Approaches for Polycrystalline Aggregates

Igor Simonovski[1] and Leon Cizelj[2]

[1]*European Commission, DG-JRC, Institute for Energy and Transport,*
P.O. Box 2, NL-1755 ZG Petten
[2]*Jožef Stefan Institute, Reactor Engineering Division, Jamova cesta 39, SI-1000 Ljubljana*
[1]*The Netherlands*
[2]*Slovenia*

1. Introduction

In polycrystalline aggregates microstructure plays an important role in the evolution of stresses and strains and consequently development of damage processes such as for example evolution of microstructurally small cracks and fatigue. Random grain shapes and sizes, combined with different crystallographic orientations, inclusions, voids and other microstructural features result in locally anisotropic behavior of the microstructure with direct influence on the damage initialization and evolution (Hussain, 1997; Hussain et al., 1993; King et al., 2008a; Miller, 1987). To account for these effects grain-scale or meso-scale models of polycrystalline aggregates are being developed and are increasingly being used.

In this chapter we present some of the most often used approaches to modeling polycrystalline aggregates, starting from more simplistic approaches and up to the most state-of-the art approaches that draw on the as-measured properties of the microstructure. The models are usually based on the finite element approach and differ by a) the level to which they account for the complex geometry of polycrystalline aggregates and b) the sophistication of the used constitutive model. In some approaches two dimensional models are used with grains approximated using simple geometrical shapes like rectangles (Bennett & McDowell, 2003; Potirniche & Daniewicz, 2003) and hexagons (Sauzay, 2007; Shabir et al., 2011). More advanced approaches employ analytical geometrical models like Voronoi tessellation in 2D (Simonovski & Cizelj, 2007; Watanabe et al., 1998) and 3D (Cailletaud et al., 2003; Diard et al., 2005; Kamaya & Itakura, 2009; Simonovski & Cizelj, 2011a). In the most advanced approaches, however, grain geometry is based on experimentally obtained geometry (Lewis & Geltmacher, 2006; Qidwai et al., 2009; Simonovski & Cizelj, 2011b) using methods such as serial sectioning or X-ray diffraction contrast tomography (DCT) (Johnson et al., 2008; Ludwig et al., 2008). These approaches are often referred to as "image-based computational modeling" and can also embed in the model measured properties such as crystallographic orientations. The acquired information is of immense value for advancing our understanding of materials and for developing advanced multiscale computational models. The rather high level of available details may render extremely complex geometries, resulting in highly challenging preparation of finite element (FE) models (Simonovski & Cizelj, 2011a) and computationally extremely demanding simulations. These two constraints have so far limited the development and use

of the image-based models. Steps aimed at obtaining a 'reasonable' size model in the terms of computational times are presented. The term 'reasonable' should be taken in relative terms as these models may still run for several days on today's high performance clusters.

Specifically, two analytical approaches (two and three dimensional Voronoi tessellations) for modeling grain geometries as well as an approach based on the X-ray diffraction contrast tomography (DCT) (Johnson et al., 2008; Ludwig et al., 2008) are presented. The DCT enables spatial non-destructive characterization of polycrystalline microstructures (King et al., 2010). The process of building a finite element model from either analytical spatial structures or as-measured spatial structures is explained. The meshing procedure, including ensuring conformal mesh between the grains as well as grain boundary modeling are discussed and explained. The most used constitutive models and the issues related to the modeling of the grain boundaries using the cohesive zone approaches are discussed. In the last section the effects of grain structure to inhomogeneous stress/strain distribution is demonstrated. Initiation and development of intergranular stress corrosion cracks is outlined and discussed for different constitutive models. Also, the stability of the simulations and measures aimed at improving it are considered.

2. Analytical models of structures

In material science Voronoi tessellations are extensively used to model grain geometry with the purpose of calculating the properties of polycrystalline aggregates (Cailletaud et al., 2003; Kovač & Cizelj, 2005), modeling short crack initiation and propagation or modeling intergranular stress corrosion cracks (Kamaya & Itakura, 2009; Musienko & Cailletaud, 2009; Simonovski & Cizelj, 2011b). A Voronoi tessellation is a cell structure constructed from randomly positioned points, also referred to as Poisson points. For polycrystalline aggregates we can think of these points as points where the solidification starts and then uniformly extends in all directions. A solidification front then expands until it collides with another one, thus creating a grain boundary. In geometrical terms the grain boundary is obtained by introducing lines perpendicular to lines connecting neighboring Poisson points. The result is a set of convex polygons/polyhedra, see Fig. 1. Examples of 2D Voronoi tessellations can be seen in Fig. 2. Additional details on mathematical background and applications are available in (Aurenhammer, 1991; Okabe et al., 2000).

Three dimensional Voronoi tessellations can be created using the same approach. A number of mathematical and programming packages like Matlab have the option of constructing such tessellations. Fig. 3 shows examples of 3D Voronoi tessellations generated using Qhull algorithm (*Qhull code for Convex Hull, Delaunay Triangulation, Voronoi Diagram, and Halfspace Intersection about a Point*, n.d.) and implemented in (Petrič, 2010).

3. As-measured spatial structures

Models of polycrystalline aggregates can also be created from the experimental data, where the grain shapes and orientations are measured, i.e. the microstructure is being characterized. A widely used method for characterizing the microstructure in order to get the data for creating a finite element model is serial sectioning (Lewis & Geltmacher, 2006; Qidwai et al., 2009; Spowart et al., 2003). With this approach a surface of the specimen is characterized and then a thin layer of material is removed to be able to characterize the next layer. The procedure is consecutively repeated, thus obtaining the data at different depths. The 3D
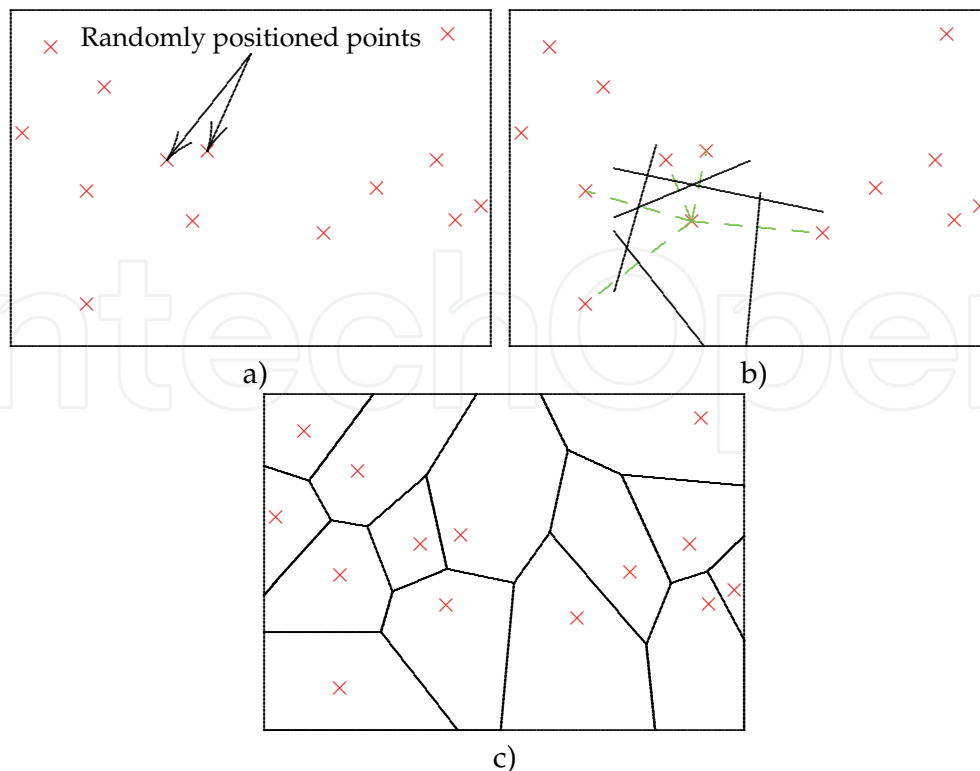
Fig. 1. Construction of a Voronoi tessellation in 2D: a) Poisson points, b) perpendicular lines are introduced to lines connecting neighboring Poisson points and c) final Voronoi tessellation.
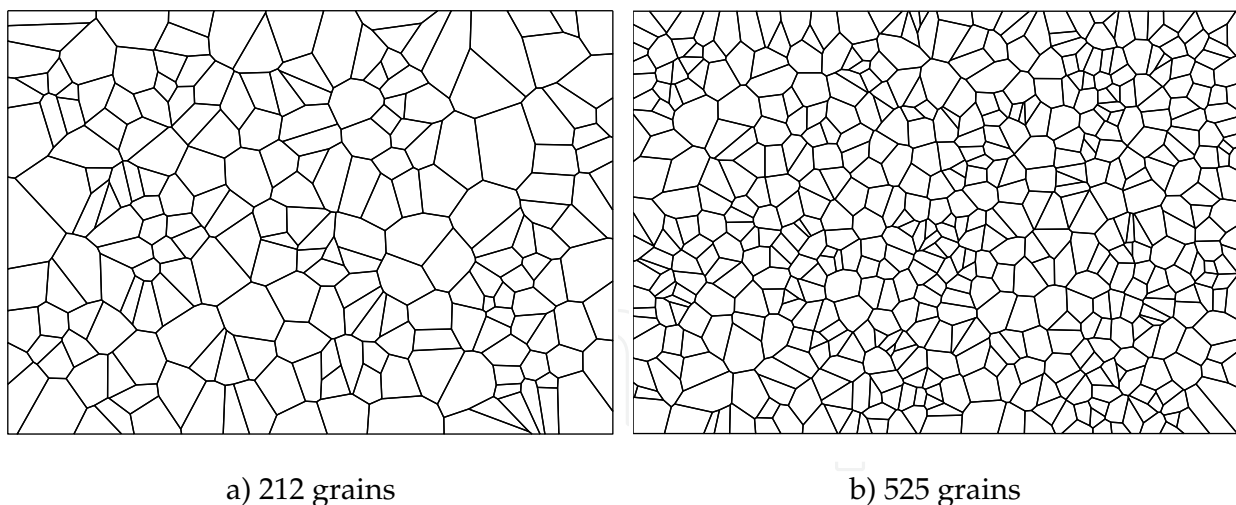

a) 212 grains   b) 525 grains

Fig. 2. Examples of 2D Voronoi tessellations.

shapes of the grains are then reconstructed from the data from the 2D layers. However, the problem with this approach is that the specimen is destroyed during the measurement procedure. In last years new experimental techniques have enabled non-destructive spatial characterization of polycrystalline aggregates. Differential aperture X-ray microscopy (Larson et al., 2002), 3D X-ray diffraction microscopy (3DXRD) (Poulsen, 2004) and X-ray diffraction contrast tomography (DCT) (Johnson et al., 2008; Ludwig et al., 2008) are examples of these

100 grains   500 grains

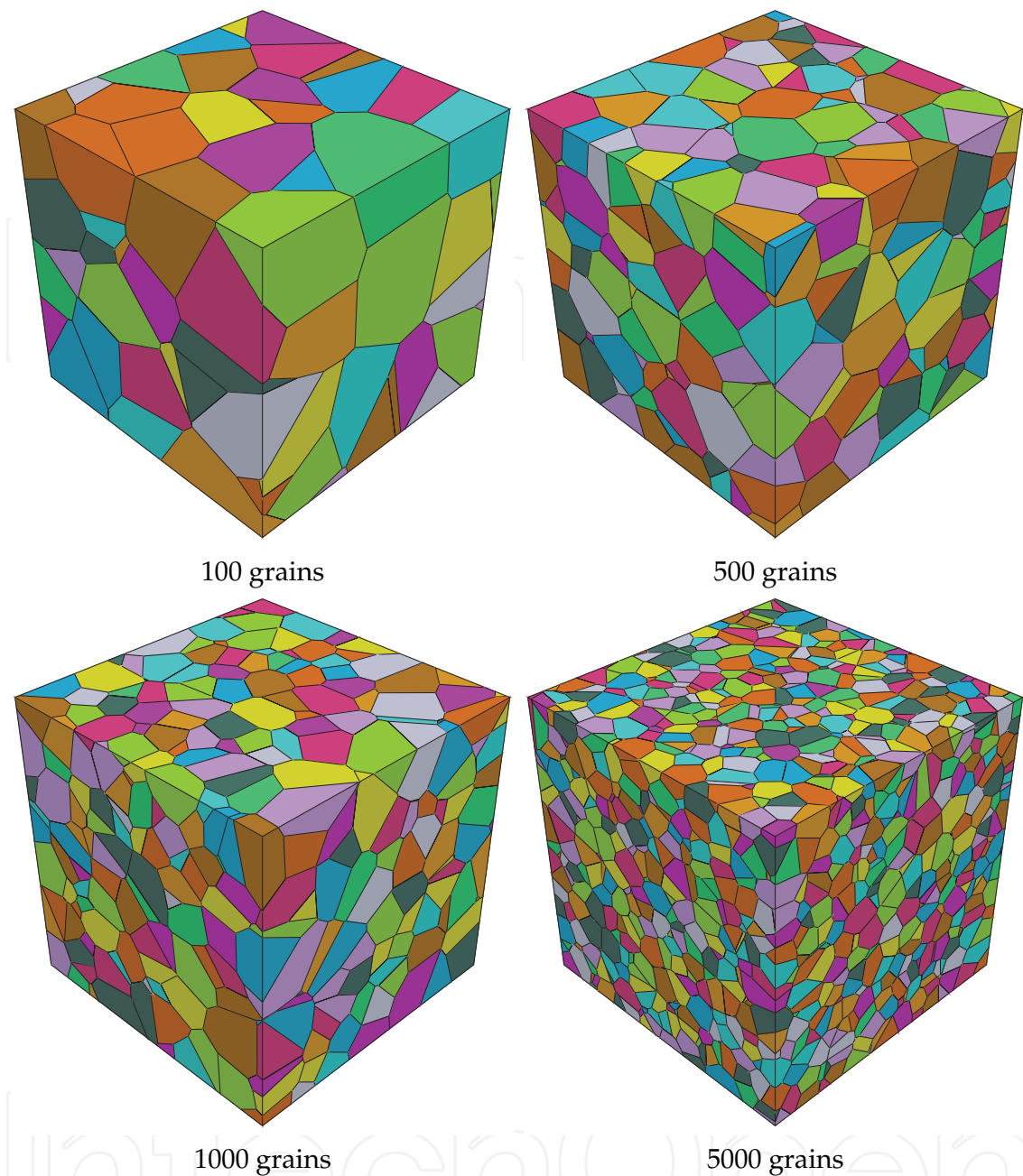1000 grains   5000 grains

Fig. 3. Examples of 3D Voronoi tessellations.

procedures. Through DCT for example, grain shapes and orientations can be measured and even crack initiation and growth can be monitored (Herbig et al., 2011). Since for some of the presented cases the data has been acquired using DCT, the next section gives an overview of this technique.

3.1 X-ray diffraction contrast tomography (DCT)

DCT (King et al., 2008a; Ludwig et al., 2008) is a measurement procedure jointly developed by the European Synchrotron Radiation Facility (ESRF) and University of Manchester, Materials Performance Centre, School of Materials. It combines the X-ray diffraction imaging and image reconstruction from projections to obtain the data on the grain shapes and crystallographic
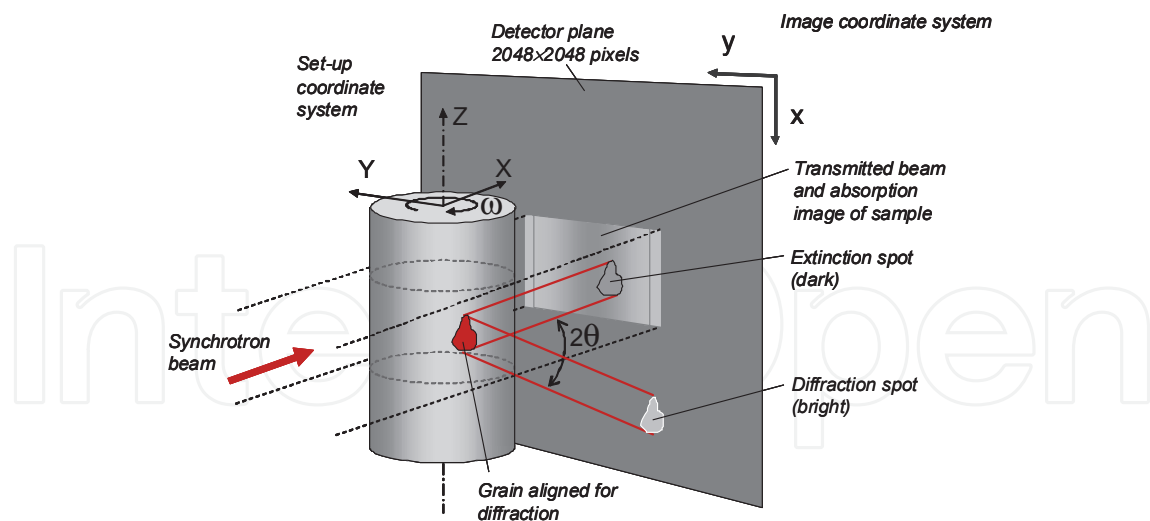
Fig. 4. A scheme of X-ray diffraction contrast tomography (DCT), after (Johnson et al., 2008).

orientations. A rotating polycrystalline sample is exposed to a monochromatic X-ray wave while the projection images are recorded, Fig. 4. Since the sample is rotating, each grain will pass through Bragg diffraction alignments several times. A detector system, significantly bigger than the sample, captures low index reflections. In absence of orientation and strain gradients within the grains, the diffracted beams form 2D spots that can be treated as parallel projections of the grains' volume (King et al., 2010). The shape of each grain can then be reconstructed in 3D using algebraic reconstruction techniques (Gordon et al., 1970). The resolution of the technique is in the order of $1\,\mu$m. An example of a measured grain shape of a $400\,\mu$m diameter stainless steel wire is given in Fig. 5. The complete wire is depicted in Fig. 6.
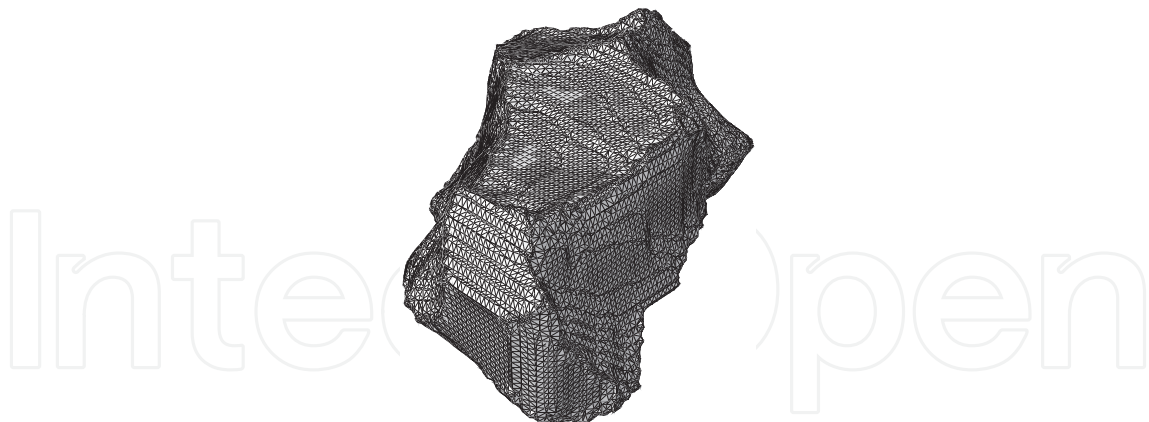

Fig. 5. An example of a measured grain shape. Full resolution is used.

One can see that the available level of detail is very high and that the obtained geometry is extremely complex. This results in highly challenging preparation of finite element (FE) models and computationally extremely demanding simulations. These two constraints have so far limited the development and use of the image-based models. However, with suitable simplifications and parallel pre-processing (Simonovski & Cizelj, 2011a), appropriate FE models can be built in a reasonable time.
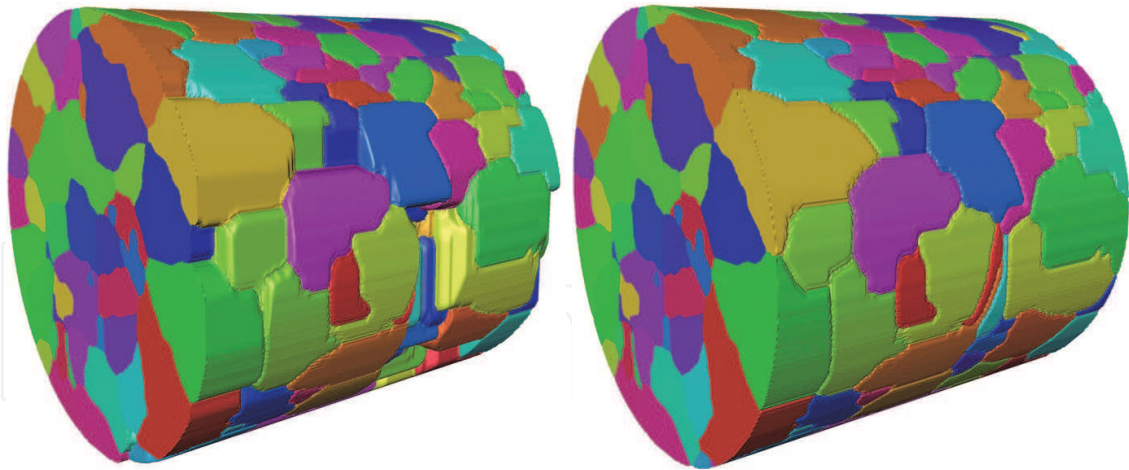
Fig. 6. Reconstructed geometry of a 400 μm diameter stainless steel wire. Left: holes in the original experimental data. Right: wire after the hole treatment, surface grooves present.

3.2 Experimental data

The experimental data used in this work is of a 400 μm diameter stainless steel wire characterized in 3D by DCT (King et al., 2008a). The data has been kindly provided by the University of Manchester, Materials Performance Centre, School of Materials and comprises of 362 grains and some 1600 grain boundaries. The data provides information on the crystallographic orientation in points of a 346 by 346 by 282 grid. The experimental data can be represented as an array of 282 slices, separated in the depth (Z) direction by 1.4 μm. For each slice, crystallographic orientation has been measured on a 346 by 346 grid with 1.4 μm distance between the points on a grid (in the X and Y direction). Voxels having the same crystallographic orientation constitute a grain.

3.3 From the measured data to the surfaces

DCT characterization of a polycrystalline aggregate results in voxel-based data. Voxel-based data is also obtained in other experimental techniques like computed tomography (CT) or magnetic resonance imaging (MRI). To obtain the shapes of individual grains their surfaces need to be reconstructed from the voxel-based data.

3.3.1 Treatment of holes

The original DCT data contains 'holes' in the reconstructed grains, see the left-hand-side of Fig. 6. These are typical artifacts due to the limited number of projections available for each grain and the presence of erroneous contrast (Johnson et al., 2008; Ludwig et al., 2008). Since the holes are not expected in the experimental data, a simple and efficient treatment algorithm can be used to fill the holes by grain growth:

- The layers with depth of one voxel are successively added to the grains in the holes vicinity. Each layer is defined along the border between grains and holes by inspecting the one voxel deep neighborhood of the voxels within holes. Only the hole voxels with exactly one neighboring grain are added to this grain within each layer.

- Only the hole voxels with multiple neighbors remain after the first step. These are assigned to the grains dominating their immediate (one voxel deep) neighborhood.

The right-hand-side of Fig. 6 displays wire data-set after the treatment above.

3.3.2 Surface reconstruction

Geometries of individual grains need to be reconstructed from the voxel-based data. This is usually achieved through reconstructing the surfaces of individual grains. Surface reconstruction from voxels is available in a number of commercial visualization tools. The origins of these tools can mainly be traced to the field of medical visualization. The tools were later further developed for the application to material science. In this work surfaces are reconstructed as sets of triangles with Amira package (Visage Imaging GmbH, 2010). A label is assigned to each measured point, defining to which grain this point belongs. The labels are equal to the index of the crystallographic orientation. Label 1 refers to grain 1 with crystallographic orientation index 1 and so forth.

Amira's built-in SurfaceGen tool with unconstrained smoothing option is used. This tool partitions the bounding volume into 362 grains depending on the number of different labels in the 8 vertices of a given voxel. Near the triple points between the grains and near the grain boundaries vortices of a given voxel will be distributed among several grains. In these cases the voxel is subdivided into up to 6^3 sub-vortexes to give a topologically correct representation of the implicitly defined separating surfaces (Westerhoff, 2003). If two adjacent sub-vortexes are of different grains, their common face is added to the list of boundaries between the two grains. A comprehensive explanation of the procedure is given in (Stalling et al., 1998; Westerhoff, 2003) and was later implemented in Amira. Described approach automatically increases the resolution near the triple points between the grains and near the grain boundaries where vortices of a given voxel are distributed among several labels/grains. This is especially important since stress increases at these points can be expected due to different crystallographic orientations of the adjacent grains. Further details on the implemented approach can be found in (Simonovski & Cizelj, 2011a).

The density of the triangles forming the reconstructed surfaces is limited by the resolution of the experimental data. At full resolution the number of triangles is 4 758 871, resulting in FE model with 51 211 552 finite elements. The number of triangles therefore needs to be decreased. This is done using Amira's built-in surface simplification tool (Zachow et al., 2007). The simplification decreases the details as well as resolution at the triple lines between the grains, see Fig. 7 where the number of triangles has been decreased to 30 000 (case 30K), 150 000 (case 150K) and 300 000 (case 300K).

4. From surfaces to FE models

The complexity of the reconstructed surfaces, together with a rather large number of grains, essentially prevents the direct use of the finite element meshing capabilities of either Amira or even professional mesh generators such as for example ABAQUS/CAE (Simulia, 2010). A framework for the automatic meshing has been therefore developed (Simonovski & Cizelj, 2011a) using the Python scripting language and ABAQUS/CAE meshing tools, which are fully accessible through Python.

The framework can be applied to both analytical models of structures (e.g. 3D Voronoi tessellations) and to data obtained from experimental techniques. In both cases the surface structures are defined by the triangle-based surfaces, bounding the volume of individual grains. In the case of voxel-based data these surfaces are reconstructed with Amira. For
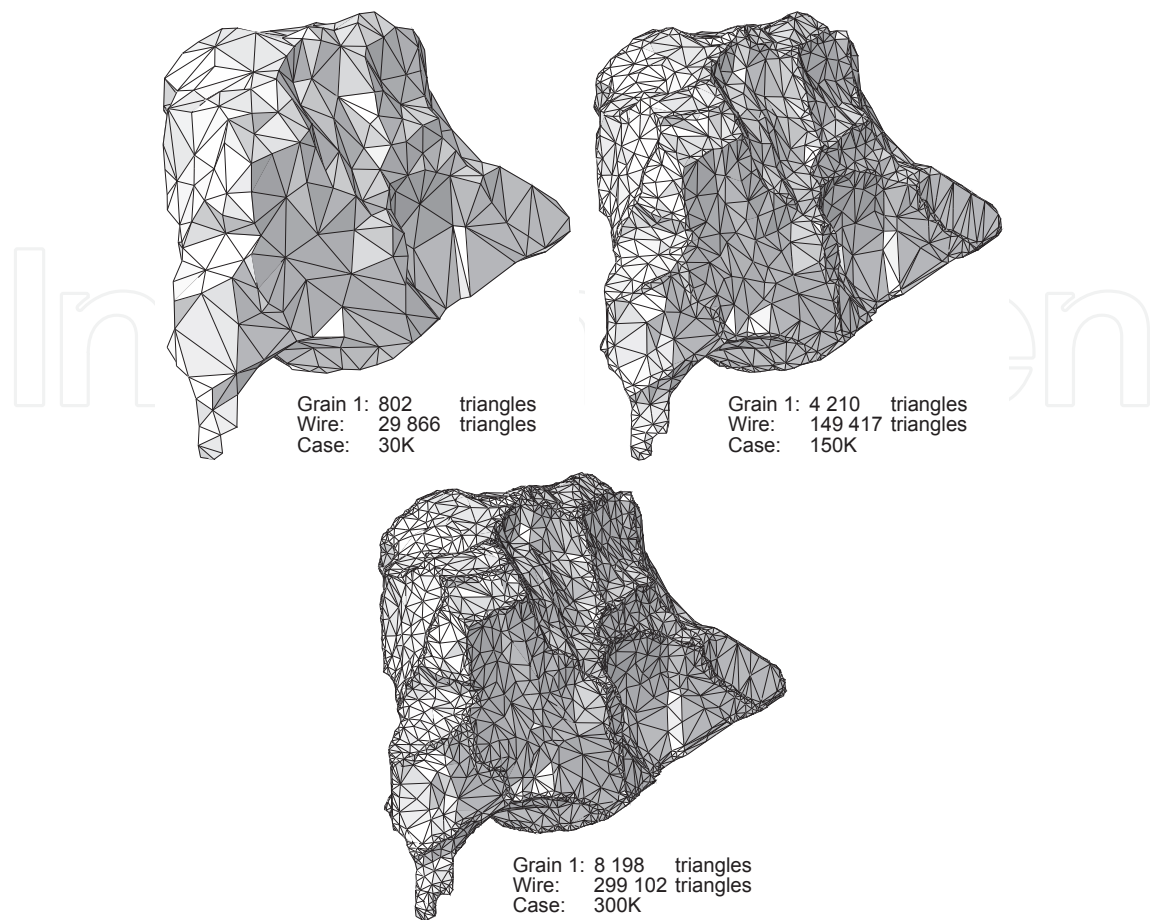
Fig. 7. Geometry reconstructed from experimental data: grain 1 from the wire data set.

analytical models such as 3D Voronoi tessellations, the spatial structure is generated by the underlying analytical model (e.g. Qhull algorithm (*Qhull code for Convex Hull, Delaunay Triangulation, Voronoi Diagram, and Halfspace Intersection about a Point*, n.d.) implemented in (Petrič, 2010)) and surface reconstruction is not needed.

Before starting the FE meshing procedure the surface triangles aspect ratios are checked. Surface triangle aspect ratio is defined in this work as the ratio of the circumscribed circle and the inscribed circle of a triangle. Triangles with aspect ratio of more than 1000 are removed by collapsing triangle's shortest edge, removing the triangle from the structure and updating the vertices and triangles. The procedure is performed iteratively until the worst aspect ratio is above 1000. This approach improves the FE mesh quality. The triangle-based surfaces are also checked for possible errors like intersections and corrected, if necessary, by slight displacement of appropriate triangle's corner points.

The ability of exporting the reconstructed surfaces into a standard CAD format that can be read by FE pre-processors is lacking in many visualization tools. Instead, the user is encouraged to use the tool's built in meshers, which often do not match the capabilities of dedicated FE mesh engines. Furthermore, FE pre-processors do not support export formats of the visualization tools. So there is a basic difficulty of importing the reconstructed geometry into FE pre-processors. This issue is circumvented here by developing a function for exporting the reconstructed surfaces into ACIS SAT file that can be imported into practically any FE pre-processor. The surfaces of each grain are therefore saved into ACIS SAT file with all

the surface triangles that they contain. Next, individual ACIS SAT file is imported into ABAQUS/CAE pre-processor, assigned seeds and its surfaces are meshed using triangular FE elements of a selected size. Mesh density is user controlled. The coarsest possible mesh is defined by the triangles of the reconstructed surface. Finer meshes can be obtained by using several FE elements per each triangle of the reconstructed surface. Meshing individual surfaces is independent upon each other which provides for an efficient parallelization of the process. A surface between the adjoining grains needs to be meshed only once since the shared surface is identical for both grains.
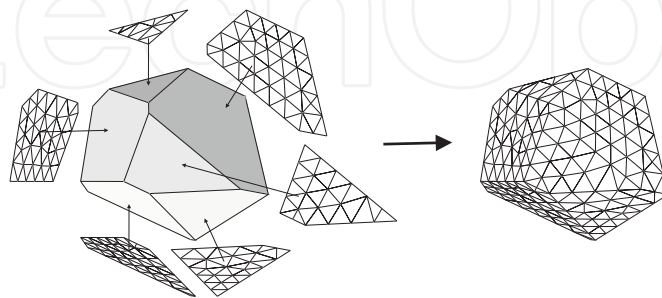

Fig. 8. Creating a conformal volume mesh between grains by meshing the grain boundary surfaces and imprinting the obtained surface meshes on the corresponding grain boundaries.
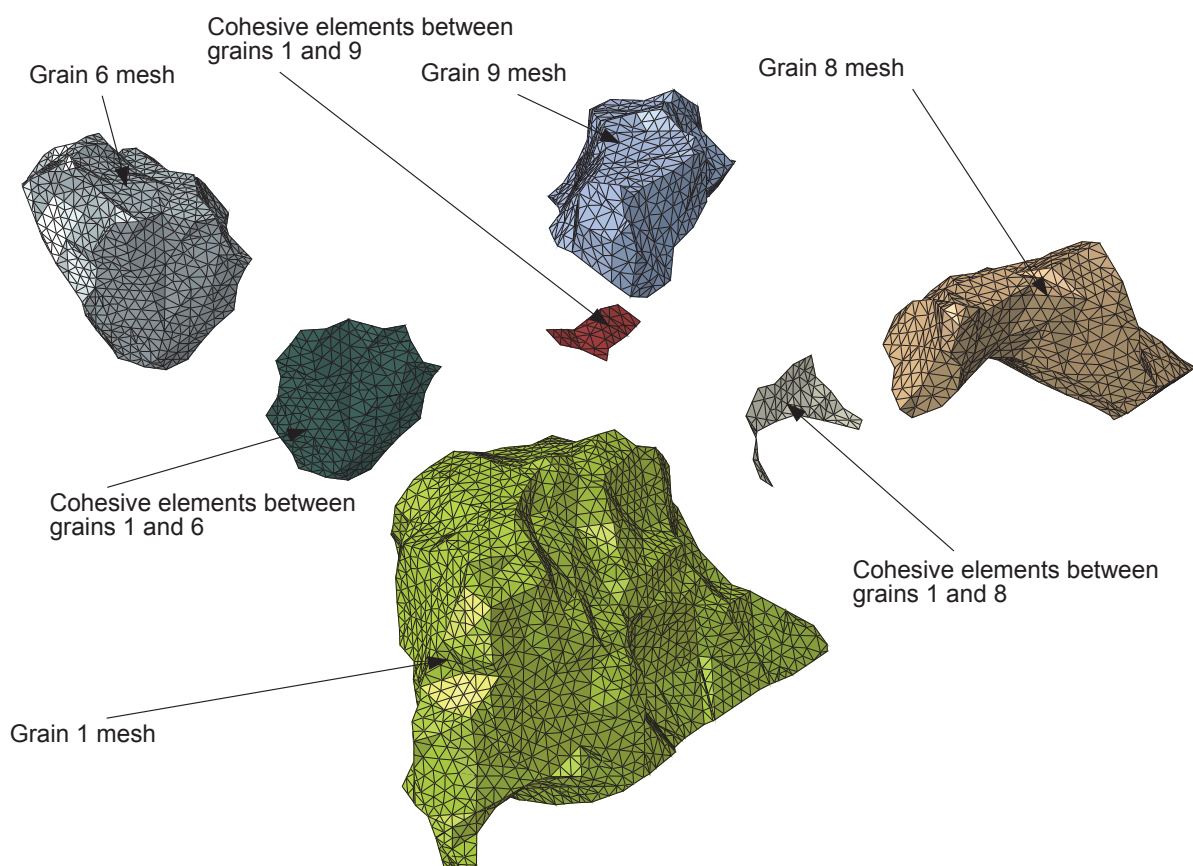

Fig. 9. Detail of the FE mesh showing cohesive elements between the grains.

To obtain a conformal mesh between adjoining grains the meshed surfaces are imprinted onto the corresponding grains, see Fig. 8. This is done by replacing the reconstructed surface of a given grain with an appropriate FE meshed surface and saving the grains' new geometry

with all the imprinted meshes into new ACIS SAT files. The process is repeated for all the grains. Updated ACIS SAT geometry files of individual grains with imprinted surface meshes are imported into a ABAQUS/CAE, assigned appropriate surface definitions, material properties, loads and boundary conditions. Exactly one FE seed per each edge is assigned to preserve the FE meshed surfaces, obtained in the previous step. The number of FE per edge is not allowed to increase/decrease thus automatically creating conformal meshes between adjoining constituents. FE volume-meshing is performed next using ABAQUS/CAE built-in mesher. All the information that has been generated in the previous steps (topology, common surfaces between the constituents, material properties,...) has been saved using the Python pickle module and is now used to hierarchically define all the properties, including node, element and surface sets. Generating FE models of individual grains is independent upon each other which again provides for an efficient parallelization.

In the last step, zero thickness layers of cohesive elements are inserted between the adjacent grains. Layers of zero thickness triangular cohesive elements are inserted between the nodes occupying the same position on the adjacent surfaces. The triangular cohesive elements are oriented to conform with the tetrahedral elements on both surfaces. The nodes, elements, set, surfaces,... and all other definitions are also updated to reflect the new configuration. Fig. 9 illustrates mesh of adjacent grains with inserted zero thickness cohesive layers. Further details on the procedures employed in automatic and parallel generation of the finite element meshes are available in (Simonovski & Cizelj, 2011a).

Fig. 10 shows the obtained FE models for the 3D Voronoi tessellations given in Fig. 3. The mesh quality factors are given in Table 1.

Fig. 11 illustrates the constructed FE model of the $400\,\mu$m diameter stainless steel wire. The top figure corresponds to the first experimental series, containing 362 grains. The model contains 903 199 finite elements: 796 105 linear solid tetrahedra elements and 107 094 cohesive elements. The bottom figure corresponds to the second experimental series, containing 1334 grains. The model contains 3 395 769 finite elements: 2 976 828 linear solid tetrahedra elements and 418 941 cohesive elements. The mesh quality factors are given in Table 2.

	100 grains	500 grains	1000 grains	5000 grains
Number of elements				
Solid elements	91 140	143 588	528 860	4 517 884
Cohesive elements	13 363	34 136	105 468	787 976
All elements	104 503	177 724	634 328	5 305 860
Number of elements with				
Min angle < 5 [°]	38 (0.0417 %)	1021 (0.7111 %)	1571 (0.2970 %)	7847 (0.1737 %)
Max angle > 170 [°]	0 (0 %)	11 (0.0077 %)	4 (0.0007 %)	27 (0.0006 %)
Aspect ratio > 10	43 (0.0472 %)	1103 (0.7682 %)	1742 (0.3294 %)	8651 (0.1915 %)
Values of				
Worst min angle [°]	2.52	0.02	0.1	0.05
Worst max angle [°]	162.09	179.9	172.5	174.27
Worst aspect ratio	27.48	1156	512.4	1028

Table 1. 3D Voronoi FE models: mesh quality factors comparison.

100 grains

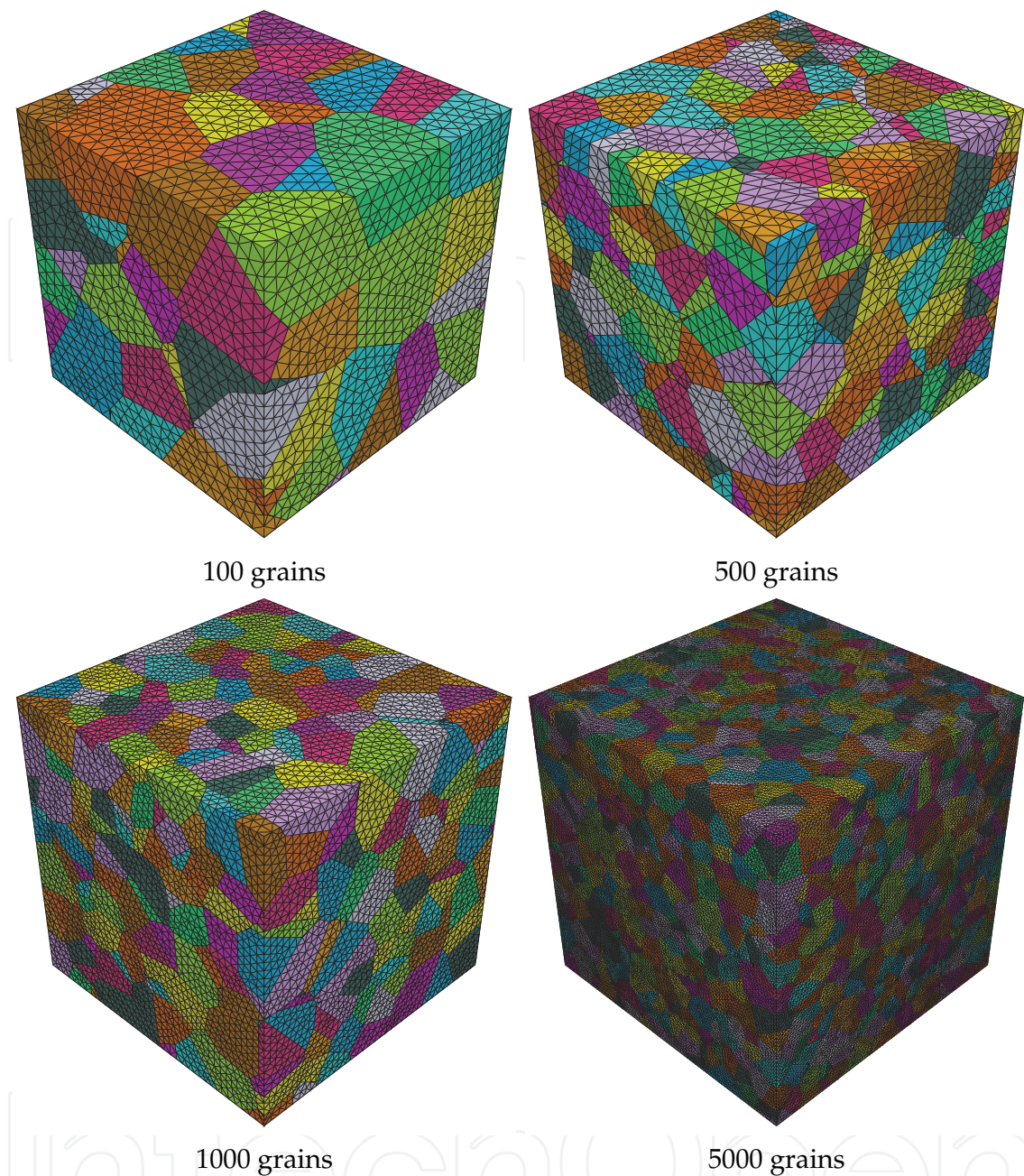500 grains

1000 grains

5000 grains

Fig. 10. FE mesh examples of 3D Voronoi tessellations.

5. Constitutive models

5.1 Bulk grains

Isotropic elasticity, anisotropic elasticity and anisotropic elasticity with crystal plasticity constitutive laws are commonly used for bulk grains. Since isotropic elasticity can not account for the effects due to different crystallographic orientations of the grains this is not covered here. Overview of the other two constitutive laws is given below.

Fig. 11. A FE model of the 400 μm diameter stainless steel wire. Top: wire from the first experimental series, 362 grains. Bottom: wire from the second experimental series, 1334 grains.

	362 grain wire	1334 grain wire
Number of elements		
Solid elements	796 105	2 976 828
Cohesive elements	107 094	418 941
All elements	903 199	3 395 769
Number of elements with		
Min angle < 5 [°]	32298 (0.2886 %)	174 (0.0058 %)
Max angle > 170 [°]	45 (0.0056 %)	12 (0.0004 %)
Aspect ratio > 10	2449 (0.3076 %)	152 (0.0051 %)
Values of		
Worst min angle [°]	0.09	0.47
Worst max angle [°]	178.77	178.64
Worst aspect ratio	647.1	23.42

Table 2. Wire FE models: mesh quality factors comparison.

5.1.1 Anisotropic elasticity

In general, the relation between the elastic stress tensor, $\sigma_{ij}^{El.}$, and the elastic strain tensor, $\epsilon_{kl}^{El.}$ for anisotropic elasticity is given by Eq. (1).

$$\sigma_{ij}^{El.} = C_{ijkl} \cdot \epsilon_{kl}^{El.} \tag{1}$$

Here, the C_{ijkl} stands for the stiffness tensor. For materials with a cubic lattice there are only three independent values in the stiffness tensor: $C_{iiii} = C_{11}$, $C_{iijj} = C_{12}$ and $C_{ijij} = C_{44}$. The relation between the strains and stresses is then given by Eq. (2).

$$\begin{Bmatrix} \sigma_{11} \\ \sigma_{22} \\ \sigma_{33} \\ \sigma_{12} \\ \sigma_{23} \\ \sigma_{31} \end{Bmatrix}^{El.} = \begin{bmatrix} C_{11} & C_{12} & C_{12} & 0 & 0 & 0 \\ C_{12} & C_{11} & C_{12} & 0 & 0 & 0 \\ C_{12} & C_{12} & C_{11} & 0 & 0 & 0 \\ 0 & 0 & 0 & C_{44} & 0 & 0 \\ 0 & 0 & 0 & 0 & C_{44} & 0 \\ 0 & 0 & 0 & 0 & 0 & C_{44} \end{bmatrix} \begin{Bmatrix} \epsilon_{11} \\ \epsilon_{22} \\ \epsilon_{33} \\ 2\epsilon_{12} \\ 2\epsilon_{23} \\ 2\epsilon_{31} \end{Bmatrix}^{El.} \tag{2}$$

5.1.2 Crystal plasticity

Crystal plasticity theory (Hill & Rice, 1972; Rice, 1970) assumes that the plastic deformation in monocrystals takes place via a simple shear on a specific set of slip planes. Deformation by other mechanisms such as for example diffusion, twinning and grain boundary sliding is here not taken into account. The combination of a slip plane, denoted by its normal m_i^α, and a slip direction, s_i^α, is called a slip system, (α). The plastic velocity gradient, $\dot{u}_{i,j}^p$, due to a crystallographic slip can be written using Eq. (3) (Needleman, 2000). The summation is performed over all active slip systems, (α), with $\dot{\gamma}^{(\alpha)}$ representing the shear rate.

$$\dot{u}_{i,j}^p = \sum_\alpha \dot{\gamma}^{(\alpha)} s_i^{(\alpha)} m_j^{(\alpha)} \tag{3}$$

The cumulative slip is defined as $\gamma = \sum_\alpha \int_0^t \left| \dot{\gamma}^{(\alpha)} \right| dt$. From the well-known relation for small strain $\epsilon_{ij} = \frac{1}{2} \left(u_{i,j} + u_{j,i} \right)$ one can obtain the plastic strain rate, Eq. (4). The constitutive relation of the elastic-plastic monocrystal is now given in terms of stress and strain rates as $\dot{\sigma}_{ij} = C_{ijkl} \left(\dot{\epsilon}_{kl} - \dot{\epsilon}_{kl}^p \right)$ (Needleman, 2000).

$$\dot{\epsilon}_{ij}^p = \sum_\alpha \frac{1}{2} \dot{\gamma}^{(\alpha)} \left(s_i^{(\alpha)} m_j^{(\alpha)} + s_j^{(\alpha)} m_i^{(\alpha)} \right) \tag{4}$$

It is assumed that the shear rate $\dot{\gamma}^{(\alpha)}$ depends on the stress only via the Schmid resolved shear stress, $\tau^{(\alpha)}$, Eq. (5) and Eq. (6). This is a reasonable approximation at room temperature and for ordinary strain rates and pressures (Needleman, 2000). Yielding is then assumed to take place when the Schmid resolved shear stress exceeds the critical shear stress τ_0.

$$\dot{\gamma}^{(\alpha)} = \dot{a}^{(\alpha)} \left(\frac{\tau^{(\alpha)}}{g^{(\alpha)}} \right) \left| \frac{\tau^{(\alpha)}}{g^{(\alpha)}} \right|^{n-1} \tag{5}$$

$$\tau^{(\alpha)} = s_i^{(\alpha)} \sigma_{ij} m_j^{(\alpha)} \tag{6}$$

$\dot{a}^{(\alpha)}$ represents the reference strain rate, n the strain-rate-sensitivity parameter and $g^{(\alpha)}$ the current strain-hardened state of the crystal. In the limit, as n approaches infinity, this power law approaches that of a rate-independent material. The current strain-hardened state $g^{(\alpha)}$ can be derived from Eq. (7), where $h_{\alpha\beta}$ are the slip-hardening moduli defined by the adopted hardening law.

$$\dot{g}^{(\alpha)} = \sum_\beta h_{\alpha\beta} \quad \dot{\gamma}^{(\beta)} \tag{7}$$

$$h_{\alpha\alpha} = \left\{ (h_0 - h_s) \operatorname{sech}^2 \left[\frac{(h_0 - h_s) \gamma^{(\alpha)}}{\tau_s - \tau_0} \right] + h_s \right\} G \left(\gamma^{(\beta)}; \beta \neq \alpha \right) \tag{8}$$

$$h_{\alpha\beta} = q h_{\alpha\alpha}, \qquad (\alpha \neq \beta), \tag{9}$$

$$G \left(\gamma^{(\beta)}; \beta \neq \alpha \right) = 1 + \sum_{\beta \neq \alpha} f_{\alpha\beta} \tanh \left(\frac{\gamma^{(\beta)}}{\gamma_0} \right) \tag{10}$$

In this work the Bassani (Bassani & Wu, 1991) hardening law is used with the hardening moduli defined with Eqs. (8, 9, 10). Here h_0 stands for the initial hardening modulus, τ_0 the yield stress (equal to the initial value of the current strength $g^{(\alpha)}(0)$) and τ_s a reference stress where large plastic flow initiates (Huang, 1991). h_s is hardening modulus during easy glide within stage I hardening and q is a hardening factor. The function G is associated with cross hardening where γ_0 is the amount of slip after which the interaction between slip systems reaches the peak strength, and each component $f_{\alpha\beta}$ represents the magnitude of the strength of a particular slip interaction. This model was implemented as a user-subroutine into the finite element code ABAQUS. Further details on the applicable theory and implementation can be found in (Huang, 1991).

5.2 Grain boundaries with cohesive zone approach

Based on the experimental observations, e.g. (Coffman & Sethna, 2008), grain boundaries are modeled with a cohesive-zone approach using cohesive elements. The traction-separation constitutive behaviour with the damage initiation and evolution as implemented in ABAQUS are used in this work. The cohesive elements are inter-surface elements of often negligible thickness, which essentially measure the relative displacements of the surfaces of adjoining continuum elements. The strains ϵ in the cohesive elements are defined using the constitutive thickness of the element T_0 (mostly different from the geometric thickness which is typically close or equal to zero) and the separations of the element nodes δ as compared to their initial unloaded positions, Eq. (11).

$$\left\{ \begin{array}{c} \epsilon_n \\ \epsilon_s \\ \epsilon_t \end{array} \right\} = \frac{1}{T_0} \left\{ \begin{array}{c} \delta_n \\ \delta_s \\ \delta_t \end{array} \right\} \tag{11}$$

The indices n, s and t denote the normal and two orthogonal shear directions of the cohesive element. The normal direction always points out of the plane of the cohesive element. The tractions on the cohesive elements are then given by Eq. (12).

$$\left\{ \begin{array}{c} t_n \\ t_s \\ t_t \end{array} \right\} = \left[\begin{array}{ccc} K_{nn} & 0 & 0 \\ 0 & K_{ss} & 0 \\ 0 & 0 & K_{tt} \end{array} \right] \left\{ \begin{array}{c} \epsilon_n \\ \epsilon_s \\ \epsilon_t \end{array} \right\} \tag{12}$$
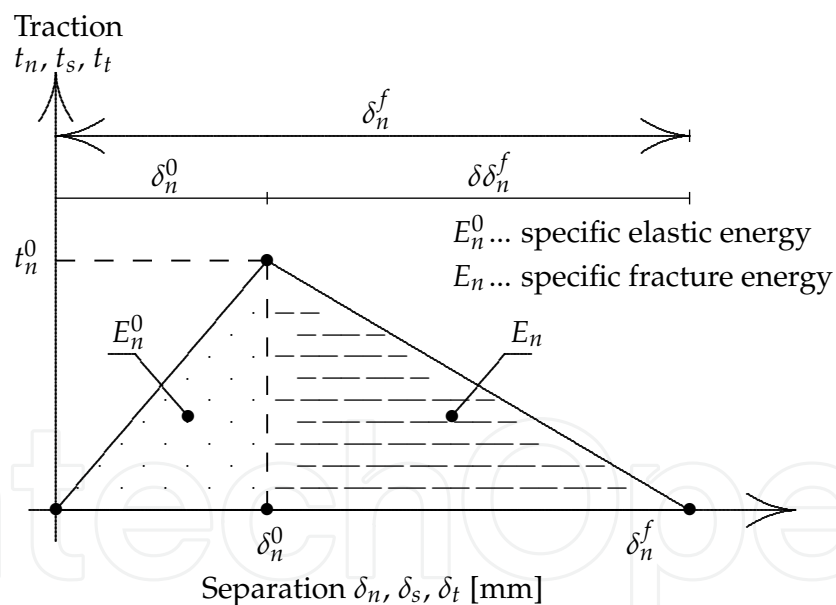

Fig. 12. Example of traction-separation response (not to scale).

Typical traction-separation response is given by Fig. 12. Damage evolution $D(\delta)$ is defined by Eq. (13) for the normal direction (and both shear directions).

$$D(\delta) = \left\{ \begin{array}{ll} 0 & ; \delta < \delta_n^0 \\ \frac{\delta_n^f \left(\delta - \delta_n^0 \right)}{\delta \left(\delta_n^f - \delta_n^0 \right)} & ; \delta \geq \delta_n^0 \end{array} \right\} \tag{13}$$

The actual load-carrying capability of the cohesive element in the normal direction would then be $[1 - D(\delta)] K_{nn}$ and correspondingly for the two shear directions.

5.2.1 Cohesive elements issues

In this section we explore the response of the cohesive elements in their normal direction. Let us have a cuboid, divided into three grains as depicted in the Fig. 13 by the three colors. Let us put 100 MPa of tensile stress on the top and the bottom surface and 200 MPa of tensile stress on the left and right surface. Let us constrain the front and the back surface in the Z direction, resulting in ϵ_{33}=0. Furthermore, let us assume that we are dealing with isotropic elastic material with Young modulus E=200 000 MPa and Poisson ratio of ν=0.3. For isotropic elastic material the Eqs. (14,15,16) are valid.
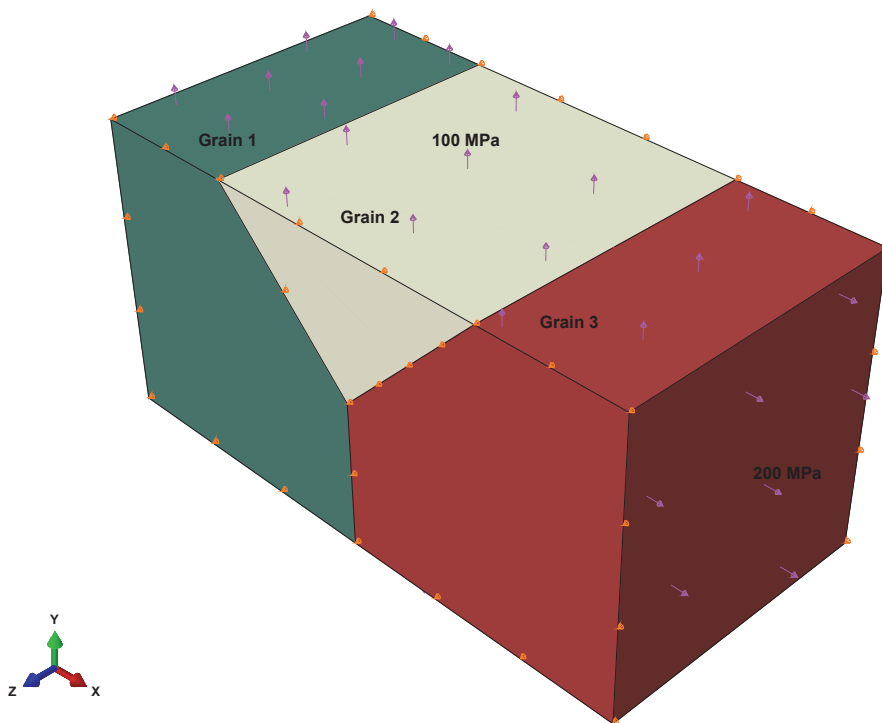

Fig. 13. A simple Y model.

$$\sigma_{11} = \frac{E}{1+\nu}\epsilon_{11} + \frac{E\nu}{(1+\nu)(1-2\nu)}(\epsilon_{11} + \epsilon_{22} + \epsilon_{33}) \tag{14}$$

$$\sigma_{22} = \frac{E}{1+\nu}\epsilon_{22} + \frac{E\nu}{(1+\nu)(1-2\nu)}(\epsilon_{11} + \epsilon_{22} + \epsilon_{33}) \tag{15}$$

$$\sigma_{33} = \frac{E}{1+\nu}\epsilon_{33} + \frac{E\nu}{(1+\nu)(1-2\nu)}(\epsilon_{11} + \epsilon_{22} + \epsilon_{33}) \tag{16}$$

From Eqs. (14,15), expressions Eq. (17,18) can be derived as ϵ_{33}=0 due to the boundary conditions. Using σ_{11}=200 MPa and σ_{22}=100 MPa we obtain values $\epsilon_{22} = 6.5 \cdot 10^{-5}$ and $\epsilon_{11} = 7.15 \cdot 10^{-4}$. Using these two values in Eq. (16) we obtain σ_{33}=90 MPa.

$$\epsilon_{22} = \frac{\sigma_{11}(1+\nu)(1-2\nu) - \sigma_{22}\frac{(1+\nu)(1-2\nu)(1-\nu)}{\nu}}{E\nu - E\frac{(1-\nu)^2}{\nu}} \tag{17}$$

$$\epsilon_{11} = \frac{\sigma_{22}(1+\nu)(1-2\nu) - \epsilon_{22}E(1-\nu)}{E\nu} \tag{18}$$

The resulting stress tensor is given by Eq. (19).

$$\sigma_{ij} = \begin{bmatrix} 200 & 0 & 0 \\ 0 & 100 & 0 \\ 0 & 0 & 90 \end{bmatrix} \text{ MPa} \tag{19}$$

The boundaries between the grain are defined with the vectors, normal to the planes of the grain boundaries.

$$n_{Grain1Grain2} = \begin{bmatrix} 1 \\ 1 \\ 0 \end{bmatrix} \cdot \frac{1}{\sqrt{2}} \tag{20}$$

$$n_{Grain2Grain3} = \begin{bmatrix} -1 \\ 1 \\ 0 \end{bmatrix} \cdot \frac{1}{\sqrt{2}} \tag{21}$$

$$n_{Grain1Grain3} = \begin{bmatrix} 1 \\ 0 \\ 0 \end{bmatrix} \cdot \frac{1}{\sqrt{2}} \tag{22}$$

Since we know the stress tensor and the normals for these three planes, we can compute the stresses in the normal direction for each of them. For the plane between the Grain1 and Grain2
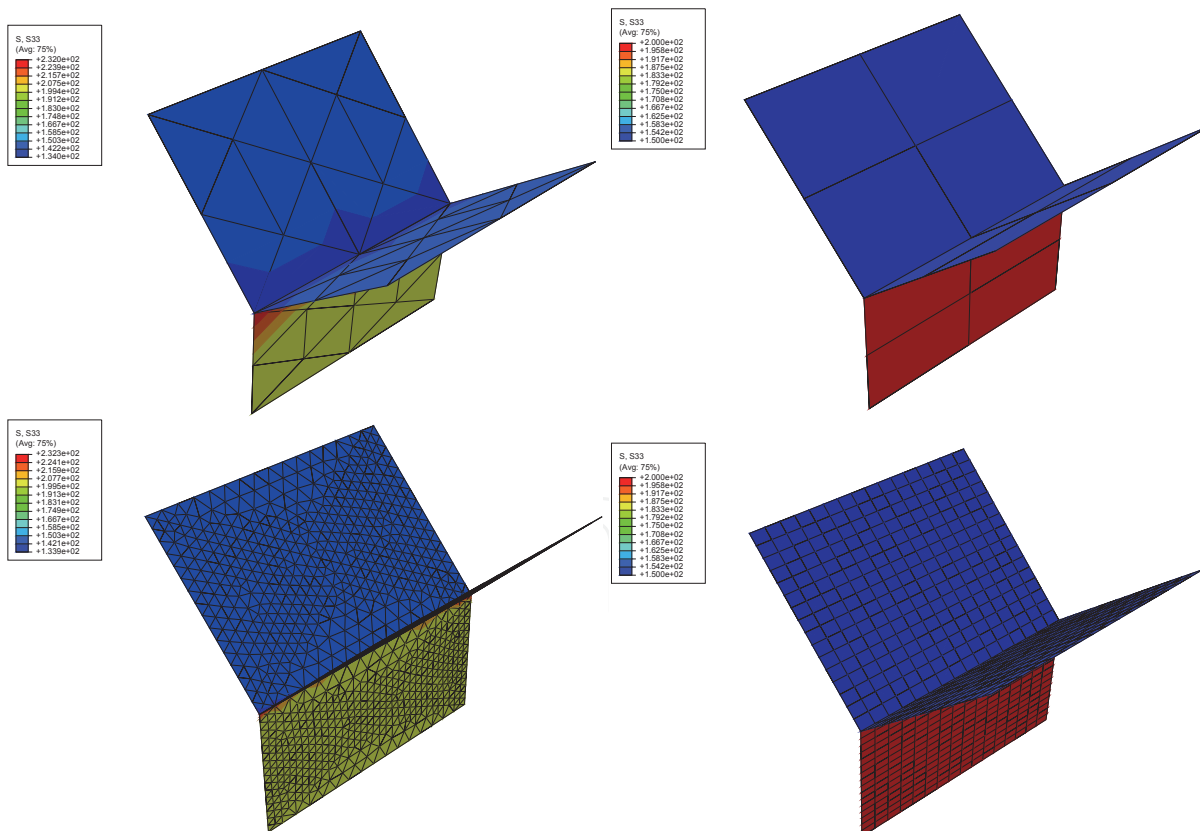

Fig. 14. Normal stresses in the cohesive elements. Triangular prisms (left) and rectangular prisms (right) cohesive elements. Variation in stress at the Y triple points can be observed for the triangular prism cohesive elements.

the stress vector on the plane, p, and the normal stress, σ_n, are given by Eq. (23) and Eq. (24).

$$Grain1Grain2: \quad p = \underbrace{\begin{bmatrix} 200 & 0 & 0 \\ 0 & 100 & 0 \\ 0 & 0 & 90 \end{bmatrix}}_{\sigma_{ij}} \cdot \underbrace{\begin{bmatrix} 1 \\ 1 \\ 0 \end{bmatrix} \cdot \frac{1}{\sqrt{2}}}_{n_{Grain1Grain2}} = \begin{bmatrix} 200 \\ 100 \\ 0 \end{bmatrix} \cdot \frac{1}{\sqrt{2}} \, \text{MPa} \tag{23}$$

$$Grain1Grain2: \quad \sigma_n = p_i \cdot n_i = 150 \, \text{MPa} \tag{24}$$

Similarly, we obtain the following normal stress values for the other two planes:

$$Grain2Grain3: \quad \sigma_n = 150 \, \text{MPa} \tag{25}$$

$$Grain1Grain3: \quad \sigma_n = 200 \, \text{MPa} \tag{26}$$

Fig. 14 displays the normal stresses in the cohesive elements as calculated from the ABAQUS finite element models. On the left hand side triangular prism cohesive elements are used, whereas on the right hand side rectangular prism cohesive elements are used. One can see that in the case of triangular prisms there is a variation in the normal stress for a given plane, in particular at the Y triple points. For the rectangular prism cohesive elements no such variations are observed and the values from the FE model match exactly with the theoretically computed values. Rectangular prism cohesive elements should therefore be preferentially used.

Unfortunately, meshing complicated shapes with rectangular prism cohesive elements also requires that the grains need to be meshed with rectangular prisms-hexahedral elements. With shapes as complicated as seen in Fig. 5 this is extremely difficult and one therefore uses triangular prisms-tetrahedral elements. This then requires the use of triangular prism cohesive elements if one is to obtain a conformal mesh between the structural and cohesive elements. One therefore automatically introduces a degree of discrepancy.

Fig. 15 displays the computed versus the theoretical normal stresses for the cohesive elements for the 3D Voronoi tessellation with 100 grains with external load of 70 MPa. Isotropic elastic constitutive law is used for the grains with the wire loaded in tension. The solid line represents the ideal response. One can observe a significant scatter from the ideal response. Fig. 16 displays the cohesive elements with red color indicating elements with more than 50 % difference between the theoretical and computed normal stresses. One can see that a significant scatter exists. Similar scatter has been reported on the grain structure simulated using 3D Voronoi tessellations (Kamaya & Itakura, 2009). Vast majority of the problematic cohesive elements are located on the triple lines between the grains. The scatter of the normal stresses of the cohesive elements not lying on the triple lines is significantly smaller, with most values within the ±20 % deviation. Increasing mesh density helps to alleviate the issue to some degree by reducing the area of the problematic elements. Other factors such as the stiffness of the cohesive element and its thickness have negligible effect on the scatter (Simonovski & Cizelj, 2011c).

6. Examples

In this section we look at the some results for the wire model with initialization and propagation of intergranular stress corrosion cracks. The grain boundaries are modeled using the above described cohesive zone approach and classified into resistant and susceptible grain
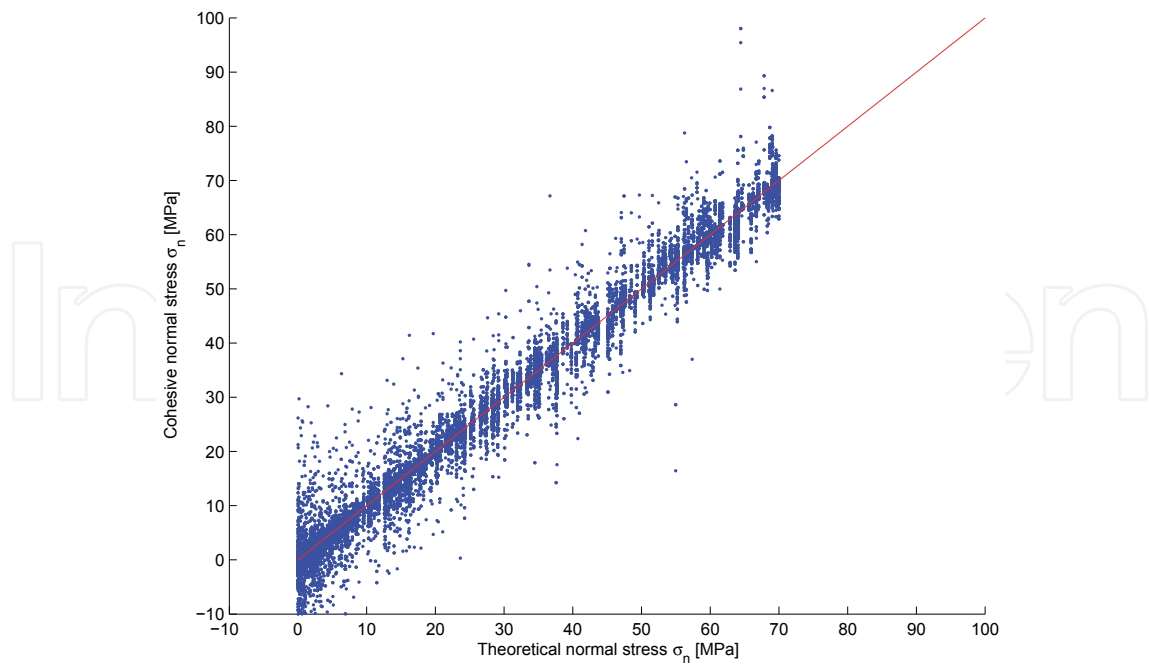
Fig. 15. Theoretical and computed normal stresses at integration points of the cohesive elements. 3D Voronoi, 100 grains, element size=0.025.
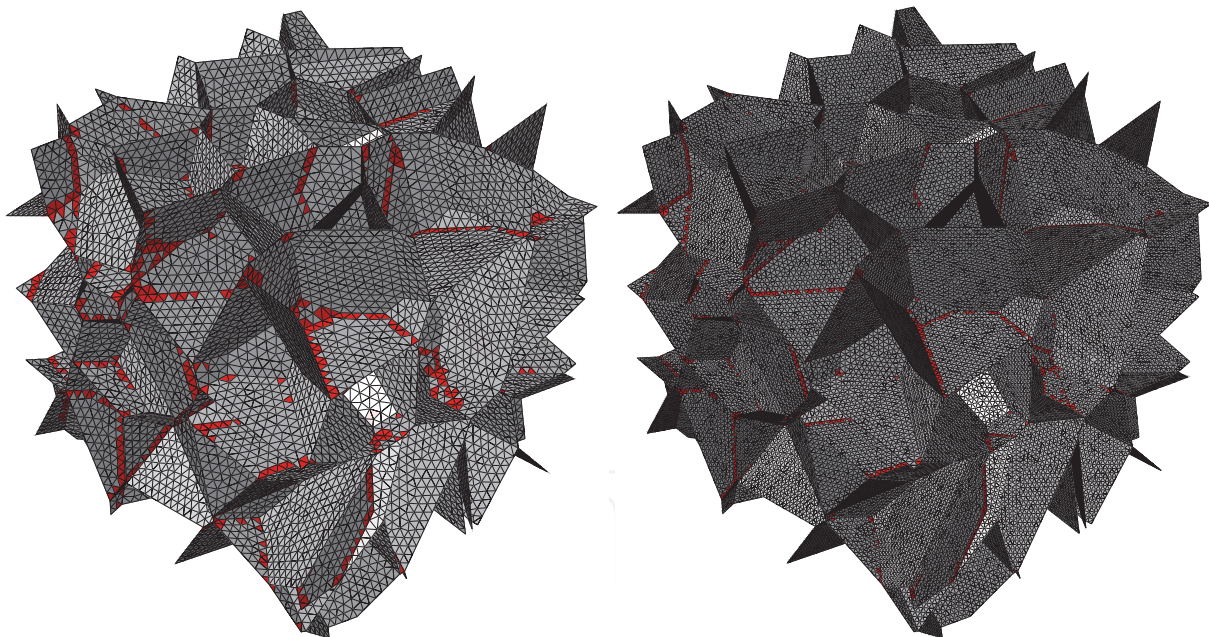

Fig. 16. Cohesive elements with more than 50 % difference between the theoretical and computed normal stresses (in red). 3D Voronoi, 100 grains. Left: element size=0.025. Right: element size=0.0125.

boundaries, depending upon the crystallographic orientation of the neighboring grains. In this work a simplification is used where resistant grain boundaries are defined as coincidence site lattice (Grimmer et al., 1974) ($\Sigma3$ through $\Sigma29$) grain boundaries and low angle grain boundaries with misorientation angle between the neighboring grains below 15°, following (Marrow et al., 2006). Σ value is computed as the ratio enclosed by a unit cell of the

coincidence sites and the standard unit cell (Bollman, 1982) from the Rodrigues vectors of the two neighboring grains. Brandon (Brandon, 1996) criterion for a proximity to a coincidence site lattice structure with proportionality constant of 10° is used. All other grain boundaries are defined as susceptible grain boundaries.

First, we constrain the nodes on the back surface in all three directions. Next, we apply tensile stress of $60\,MPa$ to the wire's front surface. This load is equal to the one in the experiment (King et al., 2008a;b). After the application of the load we assume that the wire is exposed to an acidified solution of potassium tetrathionate ($K_2S_4O_6$) that penetrates into the wire and degrades the susceptible grain boundaries. This is done to mimic the experiment and is accomplished by employing a user-defined field variable of a cylindrical shape with it's axis aligned with the wire's axis.

The radius of the user-defined field variable cylinder is progressively decreased. Once a cohesive element of a susceptible grain boundary lies outside the user-defined field variable cylinder's radius, its δ_n^0 and $\delta\delta_n^f$ values are decreased, resulting in practically instantaneous full degradation.

Damage of a cohesive element of a susceptible grain boundary that is inside the user-defined field variable cylinder's radius is caused only by mechanical overload, as depicted in Fig. 12. The described approach is purely mechanical. To improve convergence, the decrease of δ_n^0 and $\delta\delta_n^f$ values is not done abruptly. Additionally, a viscous damping of 0.01 is applied to the damage function to improve the convergence during the cohesive elements damage evolution. Susceptible grain boundaries at initial and end $10\,\%$ of the wire's length are not allowed to be affected by the user-variable to reduce the edge effect and improve the numerical stability.

The rate at which the radius of the user-defined field variable decreases (i.e. degradation rate) is linked to the stability of the computation. If a large value is selected, then within one computational time increment the separation of the opposite faces in a cohesive element can reach the critical value of δ_n^f at which the element completely degrades. If this degradation process occurs within one computational time increment, the convergence is degraded, even more so when this occurs simultaneously in several cohesive elements. Small enough degradation rates therefore need to be used, so that the process of degradation of cohesive elements is captured within the computational time increments. Alternatively, one can select very small computational time increments or increase the step time. Similarly, the δ_n^0 and $\delta\delta_n^f$ values should not be very small since at already small load increment the resulting separation of the cohesive element faces could be high enough to instantaneously completely damage the element, again causing convergence issues.

Fig. 17 shows the Mises stresses in bulk grains (left part) and damage evolution on the grain boundaries (right part) for the three constitutive models for grains. 30K case with $10.0\,\mu m$ element size is presented. The first two rows (with the exception of the legend) display the results at an early time increment where the damage due to the corrosion is very limited. For the Mises stress significant differences can be observed between the IE (isotropic elasticity) and AE (anisotropic elasticity) constitutive laws. This is to be expected since the crystallographic orientations are disregarded in IE approach. Due to the low applied load (less than 1/3rd of the yield stress) almost no difference can be observed between the Mises stresses for the AE and AE+CP (anisotropic elasticity+crystal plasticity) constitutive models. This was true even at the end of the simulation where the damage of the grain
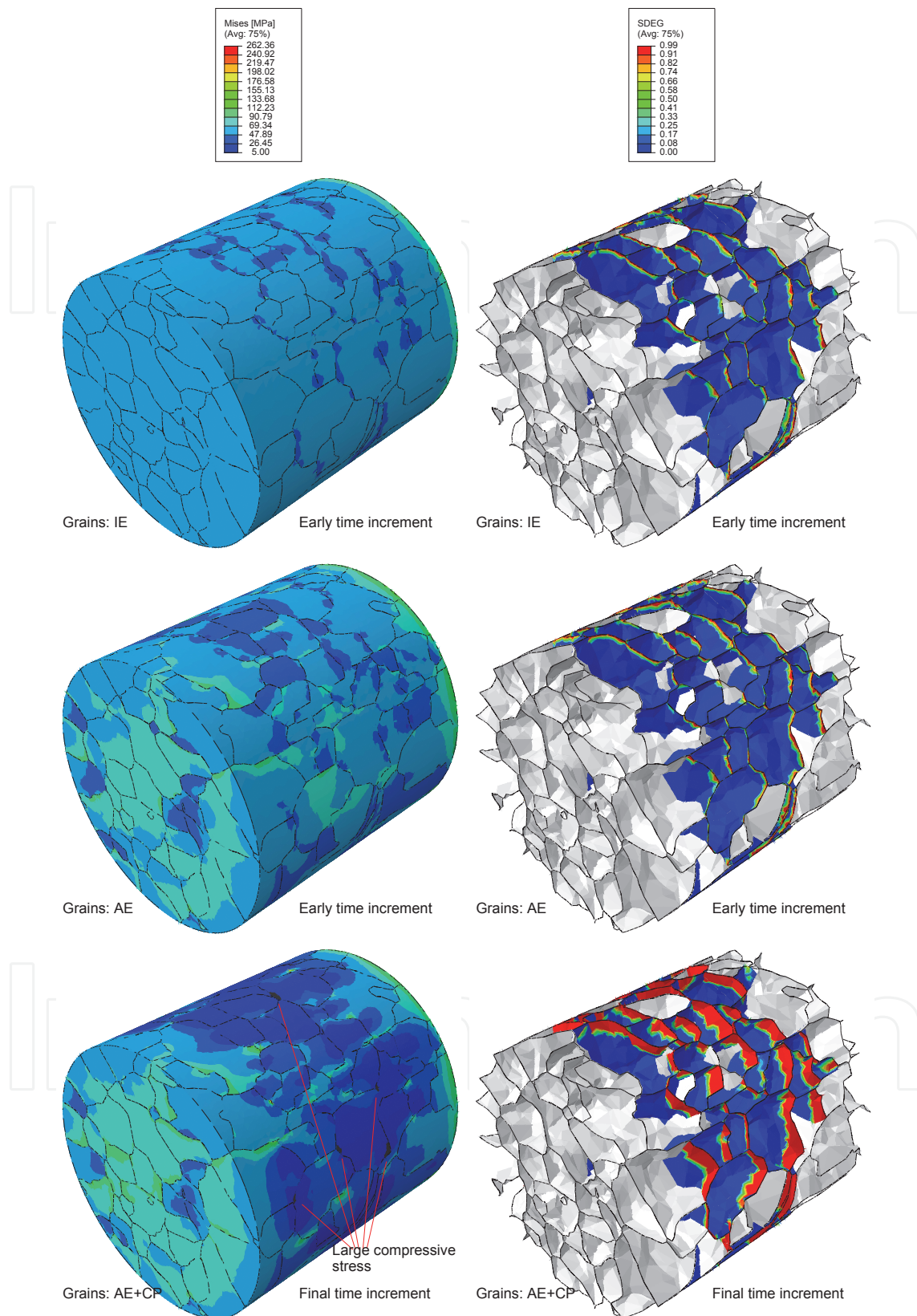
Fig. 17. Mises stress (left) and damage (right) development. Isotropic elastic (top), anisotropic elastic (middle) and anisotropic elastic + crystal plasticity model (bottom).

boundaries was at its highest, resulting in stress redistribution from the failed areas of grain boundaries to the neighboring areas of grains. The last row therefore displays only the Mises stress for the AE+CP model. Redistribution of the Mises stress can be observed due to the degradation of the susceptible, tensile-loaded grain boundaries which decreases the amount of stress transferred from one side of the boundary to the other. Stress is redistributed in the neighboring areas of grain boundaries and grains, increasing the compressive loading. This can be seen as dark patches in the last row.

The presented approach is, however, not without its deficiencies. First, all tensile-loaded grain boundaries degrade at the same rate. In reality, higher degradation rates might be expected for the susceptible grain boundaries with higher tensile load. Also, the initial grain boundary stiffness is taken to be uniform whereas stiffness distribution based upon the properties of adjacent grains is expected (Coffman & Sethna, 2008). Lastly, the selected corrosive environment penetration approach does not account for the topology of the grain boundary network. These issues will therefore need to be addressed in future work. Slightly better convergence of the AE+CP model was observed. However, the computational times for the AE+CP model were more than twice those for the AE model, see Table 3.

	AE	AE+crystal plasticity
30K case, 60 processor cores used		
Wallclock time [s]	252 005	531 133
Memory for min I/O	≈40 GB	≈80 GB
Number of elements	903 199	903 199

Table 3. Model performance data. $10.0\,\mu$m element size.

7. Conclusion

With the rapid development of computational capabilities and new experimental techniques we are moving closer to understanding the full role of microstructure on the materials performance. Not only are advanced approaches for simulating microstructures being used but also models of as-measured structures are actively being developed. Among the former, tools such as the presented 2D and 3D Voronoi tessellations can be used whereas for the latter, experimental techniques such as the X-ray diffraction contrast tomography which enable 3D characterization of grains are indispensable. Basics of these approaches are covered here. Both approaches share a common difficult task of creating a finite element model in terms of both appropriate meshes and model sizes. Surface reconstruction issues and complex geometry make the process more difficult. The presented approach effectively deals with some of these issues. The others, however, remain and are subject to further work and research.

The demonstration of the approach is presented on several cases of 3D Voronoi tessellations and two cases of a $400\,\mu$m diameter stainless steel wire. In all cases the grain boundaries are explicitly modeled using the cohesive zone approach with zero physical thickness finite elements. Grain boundaries are classified into resistant and susceptible grain boundaries, depending upon the crystallographic orientation of the neighboring grains. Grain boundary damage initialization and early development is then computed for a stainless steel case for several constitutive laws, ranging from isotropic elasticity up to crystal plasticity for the bulk grain material. Since isotropic elasticity approach disregards the crystallographic orientations it should not be used in these cases. Little differences were observed between the anisotropic

elasticity and anisotropic elasticity+crystal plasticity approaches, with the latter resulting in more than twice as long computation times.

In all cases almost uniform degradation of the grain boundaries is observed. This is attributed to a) a missing link between the grain boundary load and rate at which the corrosion penetrates the grain boundaries, b) uniform grain boundary stiffnesses whereas stiffness distribution based upon the properties of adjacent grains is expected (Coffman & Sethna, 2008) and c) the selected corrosive environment penetration approach does not account for the topology of the grain boundary network. These issues are the subject of further work.

The numerical stability of the simulation including damage is reasonable, with slightly better convergence for the anisotropic elasticity+crystal plasticity approach. The degradation of a cohesive element is linked to the stability of a simulation. If this degradation process occurs within one computational time increment, the convergence is degraded, even more so when this occurs simultaneously in several cohesive elements. Small computational time increments should therefore be used. Similarly, the δ_n^0 and $\delta\delta_n^f$ values should not be very small since at already small load increment the resulting separation of the cohesive element faces could be high enough to instantaneously completely damage the element, again causing convergence issues.

8. Acknowledgments

9. References

Aurenhammer, F. (1991). Voronoi diagrams-a survey of a fundamental geometric data structure, *ACM Computing Surveys* 23(3): 345–405.

Bassani, J. L. & Wu, T.-Y. (1991). Latent hardening in single crystals. II. Analytical characterization and predictions, *Proceedings: Mathematical and Physical Sciences* 435(1893): 21–41.

Bennett, V. P. & McDowell, D. L. (2003). Crack tip displacements of microstructurally small surface cracks in single phase ductile polycrystals, *Engineering Fracture Mechanics* 70(2): 185–207.

Bollman, W. (1982). *Crystal Lattices, Interfaces, Matrices*, Polycrystal Book Service, ISBN 2-88105-000-X.

Brandon, D. (1996). The structure of high-angle grain boundaries, *Acta Metallurgica* 14(11): 1479–1484.

Cailletaud, G., Forest, S., Jeulin, D., Feyel, F., Galliet, I., Mounoury, V. & Quilici, S. (2003). Some elements of microstructural mechanics, *Computational Materials Science* 27(3): 351–374.

Coffman, V. & Sethna, J. (2008). Grain boundary energies and cohesive strength as a function of geometry (http://link.aps.org/doi/10.1103/physrevb.77.144111), *Physical review B* 77(14): 1–11.

Diard, O., Leclercq, S., Rousselier, G. & Cailletaud, G. (2005). Evaluation of finite element based analysis of 3D multicrystalline aggregates plasticity: Application to crystal plasticity model identification and the study of stress and strain fields near grain boundaries, *International Journal of Plasticity* 21(4): 691–722.

Gordon, R., Bender, R. & Herman, G. (1970). Algebraic Reconstruction Techniques (ART) for three-dimensional electron microscopy and X-ray photography, *Journal of Theoretical Biology* 29(3): 471–481.

Grimmer, H., Bollmann, W. & Warrington, D. H. (1974). Coincidence-site lattices and complete pattern-shift in cubic crystals (http://dx.doi.org/10.1107/s056773947400043x), *Acta Crystallographica Section A* 30(2): 197–207.

Herbig, M., King, A.and Reischig, P., Proudhon, H., Lauridsen, E. M., Marrow, J., Buffière, J.-Y. & Ludwig, W. (2011). 3-D growth of a short fatigue crack within a polycrystalline microstructure studied using combined diffraction and phase-contrast X-ray tomography, *Acta Materialia* 59(2): 590–601.

Hill, R. & Rice, J. R. (1972). Constitutive analysis of elastic-plastic crystals at arbitrary strain, *Journal of the Mechanics and Physics of Solids* 20(6): 401–413.

Huang, Y. (1991). A user-material subroutine incorporating single crystal plasticity in the ABAQUS finite element program, *Technical report*, Division of Applied Sciences, Harvard University (http://www.columbia.edu/~jk2079/fem/umat_documentation.pdf).

Hussain, K. (1997). Short fatigue crack behaviour and analytical models: a review, *Engineering Fracture Mechanics* 58(4): 327–354.

Hussain, K., de los Rios, E. & Navarro, A. (1993). A two-stage micromechanics model for short fatigue cracks, *Engineering Fracture Mechanics* 44(3): 425–436.

Johnson, G., King, A., Honnicke, M. G., Marrow, J. & Ludwig, W. (2008). X-ray diffraction contrast tomography: a novel technique for three-dimensional grain mapping of polycrystals. II. The combined case (http://dx.doi.org/10.1107/s0021889808001726), *Journal of Applied Crystallography* 41(2): 310–318.

Kamaya, M. & Itakura, M. (2009). Simulation for intergranular stress corrosion cracking based on a three-dimensional polycrystalline model, *Engineering Fracture Mechanics* 76(3): 386–401.

King, A., Herbig, M., Ludwig, M., Reischig, P., Lauridsen, E., Marrow, T. & Buffière, J. (2010). Non-destructive analysis of micro texture and grain boundary character from X-ray diffraction contrast tomography, *Nuclear Instruments and Methods in Physics Research Section B: Beam Interactions with Materials and Atoms* 268(3-4): 291–296.

King, A., Johnson, G., Engelberg, D., Ludwig, W. & Marrow, J. (2008a). Observations of Intergranular Stress Corrosion Cracking in a Grain-Mapped Polycrystal (http://dx.doi.org/10.1126/science.1156211, http://www.sciencemag.org/cgi/content /full/321/5887/382), *Science* 321(5887): 382 – 385.

King, A., Johnson, G., Engelberg, D., Ludwig, W. & Marrow, J. (2008b). Observations of Intergranular Stress Corrosion Cracking in a Grain-Mapped Polycrystal (http://dx.doi.org/10.1126/science.1156211, http://www.sciencemag.org/cgi/content /full/321/5887/382), *Science* 321(5887): 382 – 385.

Kovač, M. & Cizelj, L. (2005). Modeling elasto-plastic behavior of polycrystalline grain structure of steels at mesoscopic level, *Nuclear Engineering and Design* 235(17-19): 1939–1950.

Larson, B., Yang, W., Ice, G., Budai, J. & Tischler, J. (2002). Three-dimensional X-ray structural microscopy with submicrometre resolution (http://dx.doi.org/10.1038/415887a), *Nature* 415: 887–890.

Lewis, A. & Geltmacher, A. (2006). Image-based modeling of the response of experimental 3d microstructures to mechanical loading, *Scripta Materialia* 55(1): 81–85.

Ludwig, W., Schmidt, S., Lauridsen, E. M. & Poulsen, H. F. (2008). X-ray diffraction contrast tomography: a novel technique for three-dimensional grain mapping of polycrystals. I. Direct beam case (http://dx.doi.org/10.1107/s0021889808001684), *Journal of Applied Crystallography* 41(2): 302–309.

Marrow, T., Babout, L., Jivkov, A., Wood, P., Engelberg, D., Stevens, N., Withers, P. & Newman, R. (2006). Three dimensional observations and modelling of intergranular stress corrosion cracking in austenitic stainless steel, *Journal of Nuclear Materials* 352(1-3): 62–74.

Miller, K. J. (1987). The behaviour of short fatigue cracks and their initiation. Part II-A general summary, *Fatigue & Fracture of Engineering Materials & Structures* 10(2): 93–113.

Musienko, A. & Cailletaud, G. (2009). Simulation of inter- and transgranular crack propagation in polycrystalline aggregates due to stress corrosion cracking, *Acta Materialia* 57(13): 3840–3855.

Needleman, A. (2000). Computational mechanics at the mesoscale, *Acta Materialia* 48(1): 105–124.

Okabe, A., Boots, B., Sugihara, K., Chiu, S. & Chiu, S. (2000). *Spatial Tessellations: Concepts and Applications of Voronoi Diagrams*, 2 edn, Wiley.

Petrič, Z. (2010). Generating 3D Voronoi tessellations for material modeling, *Technical report*, Jozef Stefan Institute.

Potirniche, G. P. & Daniewicz, S. R. (2003). Analysis of crack tip plasticity for microstructurally small cracks using crystal plasticity theory, *Engineering Fracture Mechanics* 70(13): 1623–1643.

Poulsen, H. F. (2004). *Three-Dimensional X-Ray Diffraction Microscopy: Mapping Polycrystals and their Dynamics*, 1st edn, Springer.

Qhull code for Convex Hull, Delaunay Triangulation, Voronoi Diagram, and Halfspace Intersection about a Point (n.d.). http://www.qhull.org.

Qidwai, M., Lewis, A. & Geltmacher, A. (2009). Using image-based computational modeling to study microstructure-yield correlations in metals, *Acta Materialia* 57(14): 4233–4247.

Rice, J. R. (1970). On the structure of stress-strain relations of time-dependent plastic deformation in metals, *Journal of Applied Mechanics* 37: 728–737.

Sauzay, M. (2007). Cubic elasticity and stress distribution at the free surface of polycrystals, *Acta Materialia* 55(4): 1193–1202.

Shabir, Z., Giessen, E., Duarte, C. & Simone, A. (2011). The role of cohesive properties on intergranular crack propagation in brittle polycrystals, *Modelling and Simulation in Materials Science and Engineering* 19(3).

Simonovski, I. & Cizelj, L. (2007). The influence of grains' crystallographic orientations on advancing short crack, *International Journal of Fatigue* 29(9-11): 2005–2014.

Simonovski, I. & Cizelj, L. (2011a). Automatic parallel generation of finite element meshes for complex spatial structures, *Computational Material Science* 50(5): 1606–1618.

Simonovski, I. & Cizelj, L. (2011b). Computational multiscale modeling of intergranular cracking (http://dx.doi.org/10.1016/j.jnucmat.2011.03.051), *Journal of Nuclear Materials* 44(22): 243–250.

Simonovski, I. & Cizelj, L. (2011c). Towards Modeling Intergranular Stress Corrosion Cracks on Grain Size Scales (submitted for publication), *Nuclear Engineering and Design* .

Simulia (2010). *ABAQUS 6.10-1 (http://www.simulia.com/)*.

Spowart, J., Mullens, H. & Puchala, B. (2003). Collecting and Analyzing Microstructures in Three Dimensions: A Fully Automated Approach, *Journal of the Minerals, Metals and Materials Society* 55(10): 35–37.

Stalling, D., Zöckler, M., Sander, O. & Hege, H.-C. (1998). Weighted labels for 3D image segmentation (http://opus.kobv.de/zib/volltexte/1998/383/), *Technical report*, Konrad-Zuse-Zentrum für Informationstechnik Berlin.

Visage Imaging GmbH (2010). *Amira 5.2.1 (http://www.amiravis.com/)*.

Watanabe, O., Zbib, H. M. & Takenouchi, E. (1998). Crystal plasticity: micro-shear banding in polycrystals using voronoi tessellation, *International Journal of Plasticity* 14(8): 771–788.

Westerhoff, M. (2003). *Efficient Visualization and Reconstruction of 3D Geometric Models from Neuro-Biological Confocal Microscope Scans (http://www.diss.fu-berlin.de/diss /receive/ FUDISS_thesis_000000001196)*, PhD thesis, Freie Universitat Berlin, FB Mathematik und Informatik.

Zachow, S., Zilske, M. & Hege, H.-C. (2007). 3D reconstruction of individual anatomy from medical image data: Segmentation and geometry processing (http://opus. kobv.de/zib/volltexte/2007/1072/), *Technical report*, Konrad- Zuse-Zentrum für Informationstechnik Berlin.
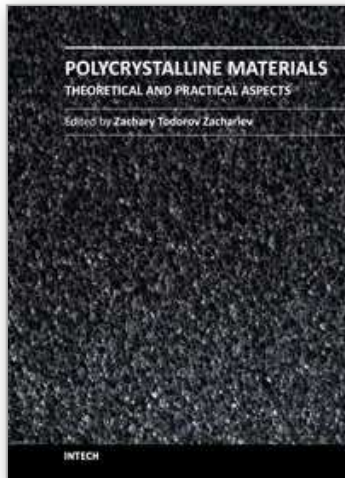
Polycrystalline Materials - Theoretical and Practical Aspects

Edited by Prof. Zaharii Zakhariev

The book "Polycrystalline Materials - Theoretical and Practical Aspects" is focused on contemporary investigations of plastic deformation, strength and grain-scale approaches, methods of synthesis, structurals, properties, and application of some polycrystalline materials. It is intended for students, post-graduate students, and scientists in the field of polycrystalline materials.

How to reference

In order to correctly reference this scholarly work, feel free to copy and paste the following:

Igor Simonovski and Leon Cizelj (2012). Grain-Scale Modeling Approaches for Polycrystalline Aggregates, Polycrystalline Materials - Theoretical and Practical Aspects, Prof. Zaharii Zakhariev (Ed.), ISBN: 978-953-307-934-9, InTech, Available from: http://www.intechopen.com/books/polycrystalline-materials-theoretical-and-practical-aspects/grain-scale-modelling-approaches-for-polycrystalline-aggregates

INTECH
open science | open minds